Modulation of cross-isothermal velocities with ENSO in the tropical Pacific cold tongue

Anna-Lena Deppenmeier* and Frank O. Bryan† and William Kessler‡ and LuAnne Thompson§

National Center for Atmospheric Research, Boulder, Colorado

*Corresponding author address: Anna-Lena Deppenmeier

E-mail: deppenme@ucar.edu

†National Center for Atmospheric Research, Boulder, Colorado

‡NOAA-PMEL, Seattle, Washington

§University of Washington,Seattle, Washington

ABSTRACT

The tropical Pacific cold tongue (CT) plays a major role in the global climate system. The strength of the CT sets the zonal temperature gradient in the Pacific that couples with the atmospheric Walker circulation. This coupling is an essential component of the El Niño Southern Oscillation (ENSO). The CT is supplied with cold water by the equatorial undercurrent that follows the thermocline as it shoals toward the east, adiabatically transporting cold water towards the surface. As the thermocline shoals, its water is transformed through diabatic processes producing water mass transformation (WMT) that allows water to cross mean isotherms. Here, we examine WMT in the cold tongue region from a global high resolution ocean simulation with saved budget terms that close its heat budget exactly. Using the terms of the heat budget, we quantify each individual component of WMT (vertical mixing, horizontal mixing, eddy fluxes, solar penetration), and find that vertical mixing is the single most important contribution in the thermocline, while solar heating dominates close to the surface. Horizontal diffusion is much smaller. During El Niño events, vertical mixing, and hence cross-isothermal flow as a whole, is much reduced, while during La Niña periods strong vertical mixing leads to strong WMT, thereby cooling the surface. This analysis demonstrates the enhancement of diabatic processes during cold events, which in turn enhances cooling of the CT from below the surface.

1. Introduction

The tropical Pacific cold tongue (CT) plays a major role in both the mean climate and climate variability. The CT is the main region of energy uptake into the ocean. It supplies buoyancy to the global circulation (Newsom and Thompson 2018; Holmes et al. 2019b), and can influence and modulate the global climate change signal (England et al. 2014). For these reasons, the mean circulation of the equatorial Pacific has historically received considerable attention: from early inferences of upwelling driven by divergence of the Ekman transport (Cromwell 1953) and the discovery of the Equatorial Undercurrent (Cromwell et al. 1954), to quantification of mass and heat budgets of the tropical cells enabled by the development of deep ocean moorings along with sparse hydrographic sections (Bryden and Brady 1985; Weisberg and Qiao 2000; Meinen et al. 2001; Johnson et al. 2001).

Sea surface temperature (SST) variability of the CT, which lies at the heart of the El Niño Southern Oscillation (ENSO), has been the focus of many studies for more than 40 years (Wyrtki 1975; Philander 1990). ENSO is the leading mode of climate variability (Neelin et al. 1998; McPhaden et al. 2006; Chang et al. 2006; Wang et al. 2017) with impacts all over the globe. Understanding the mechanisms that control the strength and variability of the CT in the tropical Pacific is essential for reliable ENSO forecasts (Ji and Leetmaa 1997; Barnston et al. 2012; Tang et al. 2018; Ding et al. 2020) and, given the importance of the eastern tropical Pacific in the global climate system, for well founded climate projections (Bayr et al. 2019; Samanta et al. 2019).

Though great progress in understanding and modeling the tropical Pacific circulation and ENSO variability has been made (Mechoso et al. 1995; Zelle et al. 2004; Karnauskas et al. 2007; Ray et al. 2018), major questions remain. For example, how does La Niña mechanistically compare to El Niño (Timmermann et al. 2018)? To what degree is SST variability driven by adiabatic (Jin

1997) versus diabatic processes (Lengaigne et al. 2012)? Often, diabatic processes have to be derived from residuals (Meinen and McPhaden 2001, 2000). Here, we employ full heat budgets from a high resolution ocean model to explicitly calculate drivers of diabatic processes.

The vertical branch of the equatorial circulation cannot be measured directly. Historically, an integrated box model approach has been taken to arrive at average upwelling estimates for large control volumes from widely spaced hydrographic sections and sparse direct velocity measurements (Wyrtki 1981; Bryden and Brady 1985; Weisberg and Qiao 2000; Johnson et al. 2001; Meinen et al. 2001). Bryden and Brady (1985) showed that a large component of the net equatorial vertical velocity is associated with the Equatorial Undercurrent (EUC) flowing parallel to isotherms as they rise toward the east, that is, a large fraction of the vertical velocity is adiabatic. Estimates of the cross-isothermal component of equatorial Pacific upwelling, again over large control volumes, based on this kinematic formulation have been made by Meinen et al. (2001) using hydrographic sections, and geostrophic and Ekman dynamics. Similar to Bryden and Brady (1985) they find that the cross-isothermal component of the vertical velocity is a fraction of the total upwelling.

However, (diabatic) ocean vertical mixing has been found to be the dominant cooling term driving SST variability in the equatorial CT on both annual and inter-annual timescales (Wang and McPhaden 1999, 2000; Moum et al. 2013; Warner and Moum 2019). There is hence a need to investigate diabatic processes and how they change during ENSO phases.

In this study, we investigate how vertical circulation in the tropics decomposes into diabatic and adiabatic flow, and how the diabatic component changes during ENSO, from global high resolution ocean model output. We employ the water mass transformation (WMT) framework, which allows us to determine how water is transformed from one water mass class into another. Here, we focus on temperature classes, i.e. water masses within a given temperature interval. In this case WMT consists of water crossing isotherms, hence we examine cross-isothermal velocities.

The WMT framework has first been developed by Walin (1982) and further illustrated by Nurser et al. (1999), who attributed the flow of water parcels across isotherms to heating and cooling. In the case of a water mass which is bound by a certain isotherm outcropping around it, heating at the surface (by surface fluxes) has to be balanced by (diffusive) cooling from below (Niiler and Stevenson 1982; Toole et al. 2004; Hieronymus et al. 2014).

Traditionally, WMT investigates heating and cooling terms over a large volume bounded by an iso-surface. Building on this we leverage an implementation of the WMT framework which allows us to calculate **local** cross-isothermal velocities and attribute them to specific diabatic processes, namely vertical mixing, solar penetration, and horizontal diffusion. Importantly, it allows us to retain spatial information about the processes.

We focus the analysis at 140°W, which is representative of the CT (marked with white cross on Fig. 2b). We also show results for other longitudes where the TAO/TRITON array (`https://www.pmel.noaa.gov/gtmba/pmel-theme/pacific-ocean-tao`) samples both the equator and at off equatorial locations (indicated with white squares on Figure 2a and b).

2. Data and Methodology

a. Model description and experimental design

We utilize output from an experiment with the ocean model "Parallel Ocean Program" (POP2) at 0.1° horizontal resolution, with 10 m thick vertical levels in the top 200 m with spacing increasing towards the bottom. The model configuration is identical to that described in Bryan and Bachman (2015). The current experiment is forced with inter-annually varying atmospheric conditions derived from the JRA-55 reanalysis (Kobayashi et al. 2015; Tsujino et al. 2018), which spans the period between 1958 and 2018. The experiment is initialised at rest with potential temperature

and salinity from World Ocean Atlas 2013 (Boyer 2013). All the terms in the temperature budget (6) at each grid point are saved during runtime as 5-day averages. The analysis presented here is restricted to the 36-year period 1983-2018, for which full heat budget output is available.

Chassignet et al. (2020) assesses the veracity of the simulation and compares it against other high-resolution global models forced under the same protocol. Here, we present temperature and zonal velocity profiles in comparison to TAO data (Fig. 1). The mean zonal flow and temperature structure along the equator are well captured, with the agreement with observations slightly better in the west (170°W) than in the east (110°W, Fig. 1). At 140°W, where we focus most of our analysis, the center of the mean EUC is 20 m deeper and 10 cm/s stronger than observed. However, the vertical shear in the upper 40-100 m is almost identical. The mixed layer in POP2 is slightly deeper than in TAO at the same location, but the thermocline is nearly equally steep (while it is a little more diffuse at 110°W). The total velocity variance (all time scales) in TAO is larger than the total variance in POP2 through the column and at all locations (compare shading around the velocity profiles in Fig. 1).

b. Analysis formulation

We diagnose volume transport across isotherms (cross-isothermal velocities, denoted w_{ci}) to investigate the processes regulating the diabatic component of the vertical circulation in the eastern tropical Pacific. The cross-isothermal velocity, w_{ci}, is defined as the difference between the velocity of the fluid in the direction normal to the isotherm and the velocity of the isotherm itself (Viúdez 2001; Groeskamp et al. 2019)

$$w_{\mathrm{ci}} \equiv \hat{\mathbf{n}}_T \cdot \left(\mathbf{u} - \mathbf{u}^{isoT}\right) \tag{1}$$

with temperature T, velocity $\mathbf{u}$, and

$$\hat{\mathbf{n}}_T = \frac{\nabla T}{|\nabla T|}. \tag{2}$$

This cross-isothermal velocity w_{ci} can be understood as an entrainment velocity that diabatically entrains water into the layer above the given isotherm. It is important to note that this is not equivalent to the entrainment velocity that is used to understand mixed layer heat budgets, since the layer here is defined by an arbitrary moving isotherm rather than a specific depth. We are hence not evaluating a heat budget in a given volume, but rather employing the connection between the heat budget and the volume budget in temperature coordinates to arrive at velocities with which water masses are transformed (cross isotherms), and identify the physical drivers behind this diabatic process. In other words, we investigate what forces water parcels to change their temperature in the Lagrangian sense.

The motion of the isotherm , $\mathbf{u}^{isoT}$, is obtained by noting that for an observer on the isotherm,

$$\frac{\partial T}{\partial t} + \mathbf{u}^{isoT} \cdot \nabla T = 0. \tag{3}$$

or

$$\mathbf{u}^{isoT} \cdot \nabla T = -\frac{\partial T}{\partial t}, \tag{4}$$

where t is time. Using the definition of the cross-isothermal direction, $\hat{\mathbf{n}}_T$, and substituting (4) in (1) gives,

$$w_{\mathrm{ci}} = \frac{1}{|\nabla T|}\left(\mathbf{u}\cdot\nabla T + \frac{\partial T}{\partial t}\right) = \frac{1}{|\nabla T|}\frac{DT}{Dt}. \tag{5}$$

Expression (5) relates the conservation of volume to the conservation of heat, a form of water mass transformation analysis. The more conventional expressions for water mass transformation relating transports to integrals of diabatic fluxes over control volumes bounded by isotherms or isopycnals (Walin 1982) can be derived from (5) (Groeskamp et al. 2019). We choose to work

with the form above to retain local information allowing us to identify where and under what flow conditions parcels cross isotherms.

This framework allows us to identify the specific processes that contribute to cross-isothermal motion by connecting the cross-isothermal velocity to the heat budget. The conservation of potential temperature (henceforth when referring to temperature we are working with potential temperature) in POP2 (Smith et al. 2010) is given by

$$\frac{DT}{Dt} = \frac{\partial}{\partial z}\left[\kappa\left(\frac{\partial T}{\partial z} - \Gamma\right)\right] - \nabla^2\left(B_h \nabla^2 T\right) + \frac{\partial}{\partial z}\left(\frac{1}{\rho_0 c_p} I\right) \tag{6}$$

with surface boundary conditions

$$\begin{aligned} \kappa \frac{\partial T}{\partial z}\Big|_{z=0} &= Q_{ns} \\ I\big|_{z=0} &= Q_s \end{aligned} \tag{7}$$

where κ is the vertical diffusivity, $\kappa\Gamma$ is the countergradient flux in the boundary layer (both diagnosed with the K-profile parameterization (KPP, Large et al. (1994), combined, the square brackets in (7) make J), B_h is the horizontal hyperdiffusivity (hence the second term on the right hand side is horizontal diffusion, $\mathbf{H}_{diff}$), ρ_0 is density, c_p is the specific heat of seawater, I is the downward radiation flux into the water column with depth z, Q_{ns} is the net non-solar component of the surface heat flux and Q_s is the surface solar heat radiation flux. Penetrative solar radiation based on climatological chlorophyll levels is calculated according to (Ohlmann 2003), based on a double exponential. Substituting the right hand side of (6) into (5) gives,

$$w_{\mathrm{ci}} = \frac{1}{\rho_0 c_p |\nabla T|}\left[\frac{\partial J}{\partial z} + \nabla \cdot \mathbf{H}_{diff} + \frac{\partial I}{\partial z}\right], \tag{8}$$

where we abbreviate the vertical and horizontal diffusive heat fluxes with J and $\mathbf{H}_{diff}$, respectively.

The derivation thus far has considered the state variables and fluxes to be instantaneous quantities. Practical applications using either observations or model output would more typically start

with quantities averaged and sampled over some finite time- and space-scales. In the analysis below, we evaluate $w_{\rm ci}$ using the temperature tendency, advective and diabatic fluxes saved as 5-day averages accumulated during the model integration. With the available archived model output we can calculate each term in (6) explicitly and satisfy the balance to roundoff error. Beginning with these averages, we use a modified version of (8) that represents the 5-day mean cross-isothermal transport across the 5-day mean position of the isotherm,

$$\begin{aligned}\overline{w}_{\rm ci} &= \frac{1}{|\nabla\overline{T}|}\left(\overline{\mathbf{u}}\cdot\nabla\overline{T}+\frac{\partial\overline{T}}{\partial t}\right)\\ &= \frac{1}{\rho_0 c_p|\nabla\overline{T}|}\left[\underbrace{\frac{\partial\overline{J}}{\partial z}}_{w^{\rm vmix}_{\rm ci}}+\underbrace{\nabla\cdot\overline{\mathbf{H}}_{diff}}_{w^{\rm hdiff}_{\rm ci}}+\underbrace{\frac{\partial\overline{I}}{\partial z}}_{w^{\rm solar}_{\rm ci}}-\underbrace{\rho_0 c_p\nabla\cdot\left(\overline{\mathbf{u}'T'}\right)}_{w^{\rm cov}_{\rm ci}}\right]+hot,\end{aligned} \tag{9}$$

where the additional term in brackets ($w^{\rm cov}_{\rm ci}$) is the resolved eddy flux of temperature on timescales less than 5 days, while higher order terms (*hot*) arise from covariance between the diabatic fluxes and the magnitude of the temperature gradient on sub-5-day timescales. With the available output we can compute the resolved sub-5-day eddy flux, but not the higher order terms. In the text below we refer to the contribution of a physical process on the cross-isothermal velocities with the notation $w^{\rm solar}_{\rm ci}$, $w^{\rm vmix}_{\rm ci}$, and so forth.

The velocities $w^{\rm solar}_{\rm ci}$ and $w^{\rm vmix}_{\rm ci}$ quantify the impact of the vertical flux divergence, rather than the flux itself (see (9)). For solar penetration, the downward flux steadily reduces with depth, hence the divergence maintains one sign. This is not true for the vertical divergence of the turbulent heat flux due to vertical mixing. For the eastern Pacific CT, the heat flux due to vertical mixing typically peaks below the surface and then further decreases with depth; thus the divergence (and therefore $w^{\rm vmix}_{\rm ci}$) is minimum where the heat flux is maximum. $w^{\rm vmix}_{\rm ci}$ can therefore have both signs. Both solar penetration and vertical mixing induce cross-isothermal velocities through their

vertical divergence. We note that when considering the cross-isothermal direction the resulting velocities can be horizontal, depending on the direction of the temperature gradient. Consider solar penetration near the surface at a vertically unstratified location. Warming the water parcel means that its location relative to the isotherm changes, from the cold side to the warm side.

The diagnostics in (9) are readily evaluated at the model grid points, for both the total w_{ci} (first row Eq. 9), and for the individual terms (second row Eq. 9). In the analysis that follows we present results in temperature coordinates. The remapping is performed by monotonic cubic spline interpolation of each term on both sides of (9) for each 5-day average prior to any additional averaging.

We examine which processes control WMT in the CT. We present results for 5°S to 5°N at 140°W, and we show the longitudinal dependence of w_{ci} for the mean field. We further examine how w_{ci} and its drivers differ between El Niño and La Niña events at 140°W. Note that the mechanisms remain the same both west and east of 140°W with the same modulations as seen in the mean field. We hence only present 140°W for the detailed analysis.

3. Results

At 140°W, in the climatological mean, cross-isothermal velocities w_{ci} are positive across the equator, indicating that cold water is transformed into warmer water. w_{ci} is maximum on the equator between 19°C and 25° with velocities up to 0.5 m/day (Fig. 2c). In the warmer temperature classes, above 22°C, water mass transformation (WMT) also occurs within 1° of latitude off the equator to the north and south. Above 24°C, the maximum cross-isothermal velocity does not occur on the equator, rather it occurs poleward of 1° (Figure 2c). A significant amount of WMT also occurs at temperatures higher than 26°C off the equator. Hatching in Fig. 2c implies that the

isotherms exist less than 50 % of the time record. The impact of temporarily existing isotherms on the results is further explained in the Discussion.

In the thermocline w_{ci} is nearly vertical, while within the mixed layer, contours of constant temperature are nearly vertical, making mixed-layer w_{ci} nearly horizontal. This is illustrated by the shape of the isotherms in Figure 2d: the 18°C-24°C isotherms are approximately horizontal, making w_{ci} approximately vertical. Isotherms above 24°C tilt indicating that $\hat{\mathbf{n}}_T$ as defined in (2) has a horizontal component. A comparison between the Eulerian (strictly vertical, w) velocity and the cross isothermal velocity w_{ci} (Fig. 2c and d) shows that both are strongest in the thermocline between 1°S-1°N, and both display a minimum on the equator near the surface.

The Eulerian velocity w is at least three times as large in the thermocline than the cross-isothermal velocity w_{ci}, consistent with findings by Meinen et al. (2001) and Bryden and Brady (1985). This is also illustrated by the profiles at 0°, 140°W (Figure 2e). Both velocities peak just above the core of EUC, where water flows east along upward sloping isotherms, and where strong shear can foster mixing (Moum et al. 1989; Lien et al. 1995; Moum and Nash 2009; Smyth and Moum 2013) which promotes WMT. Here, we confirm earlier studies that found upward motion in the equatorial Pacific consists mostly of adiabatic flow along isotherms. Like others, however, we also find that a considerable part of the upward motion is diabatic (compare diabatic w_{ci} and total vertical velocities in Fig. 2e) such that diabatic processes play a primary role in supplying cold water to the mixed layer (Meinen et al. 2001; Bryden and Brady 1985; Weisberg and Qiao 2000).

The cross-isothermal velocity, w_{ci}, cross section at 140°W (Fig. 2c) is very similar to that of other locations in the CT: centered on the equator on the colder isotherms, splitting into two maxima off the equator in the warmer isotherms (Fig. 3). The isotherms with large w_{ci} at each longitude are are constrained by the location of the EUC maximum at each longitude, hence we find w_{ci} in

warmer waters in the west and colder waters in the east. The maximum $w_{\rm ci}$ is centered north of the equator west of 125°W, and south of the equator east of 125°W.

The main drivers of WMT in the equatorial Pacific at 140°W are $w_{\rm ci}^{\rm solar}$ and $w_{\rm ci}^{\rm vmix}$ (Fig. 4). $w_{\rm ci}^{\rm hdiff}$ is orders of magnitude smaller than the other contributions (not shown), and eddy rectification effects are also insignificant in the mean derived from 5-day averaged output (not shown; note that here "eddies" refers to resolved small-scale transient motion on time scales less than 5 days which are relatively weak, tropical instability waves (TIWs) are resolved at the timescales of our calculation and their effect is included explicitly in the terms in the middle equality in (9) and implicitly through their effect on velocity shear in the mixing terms $w_{\rm ci}^{\rm vmix}$ and $w_{\rm ci}^{\rm hdiff}$).

Near the surface, $w_{\rm ci}^{\rm vmix}$ and $w_{\rm ci}^{\rm solar}$ largely cancel (compare $w_{\rm ci}$ signal in the hatched region to the signals of $w_{\rm ci}^{\rm vmix}$ and $w_{\rm ci}^{\rm solar}$ in the hatched region in Figure 4). $w_{\rm ci}^{\rm solar}$ acts to warm (Fig. 4d) the surface and therefore moves water parcels from colder to warmer classes, while $w_{\rm ci}^{\rm vmix}$ opposes $w_{\rm ci}^{\rm solar}$ and cools the surface, causing water parcels to move from warmer to colder isotherms (Fig. 4b, negative (blue) signal). In shallow layers where isotherms exist more than 50% of the time (not hatched in Fig. 4), warming by solar penetration exceeds the cooling effect of vertical mixing, leading to an overall positive signal. Note that w_{ci} very close to the surface, i.e. in the warmest isotherms, is nearly poleward, because the surface temperature gradient is dominantly meridional rather than vertical.

In the thermocline the influence of solar radiation is weak. At the 24°C isotherm on the equator and 140°W $w_{\rm ci}^{\rm vmix}$ is the dominant (and in fact single) driver of water parcels moving from colder to warmer classes (Fig. 4b). Throughout, the sum of $w_{\rm ci}^{\rm vmix}$ and $w_{\rm ci}^{\rm solar}$ almost entirely recovers the signal of $w_{\rm ci}$ (compare Fig. 4a and c). Thus, in the mean, $w_{\rm ci}^{\rm vmix}$ drives WMT across the thermocline, bringing colder water up in the thermocline, which causes cross-isothermal velocities of up to a third of the total Eulerian vertical velocity (Fig. 2e, compare blue and orange lines).

The strength of w_{ci} strongly depends on the phase of ENSO. We define El Niños in our simulation (marked in red, Figure 5a) and La Niñas (marked in blue) when a warm/cold SST anomaly above/below 0.4°C persists for at least 6 months. In the following calculations, we take averages over all events per category during the 36 year record again focusing on the results at 140°W.

During neutral conditions (Fig 5c), WMT occurs down to 20°C with w_{ci} of up to 1 m/day. During La Niña (Fig 5d), WMT is strengthened and extends down to 18°C, while during El Niño WMT transformation almost shuts down (Fig 5b). For all three phases of ENSO the balance described for the mean still holds: $w_{\mathrm{ci}}^{\mathrm{solar}}$ drives WMT in the shallowest layer, which is largely balanced by w_{ci} of opposite sign arising from $w_{\mathrm{ci}}^{\mathrm{vmix}}$ (Fig 5e&h, f&i, g&j). In the thermocline, for temperatures between 20°C and 25°C near the equator, $w_{\mathrm{ci}}^{\mathrm{vmix}}$ is responsible for nearly all cross-isothermal velocity. $w_{\mathrm{ci}}^{\mathrm{vmix}}$ is increased during La Niña (Fig 5g) and decreased during El Niño (Fig 5e) when compared to neutral conditions (Fig 5f). The variability of $w_{\mathrm{ci}}^{\mathrm{vmix}}$ explains the signal in w_{ci} (Fig 5b-d).

To illustrate in more detail the dependence of the WMT on ENSO, we show an example of the evolution of individual La Niña and El Niño events (Figure 6). During La Niña, in the cooling phase and during the phase in which cold sea surface temperatures are maintained (SST in Figure 6a blue and orange lines, w_{ci} in 6 b and c), cross-isothermal velocities are large and are driven by $w_{\mathrm{ci}}^{\mathrm{vmix}}$ (similar to what is seen in Fig 5). When SST begins to rise at the end of a La Niña (Figure 6a green line, 6d w_{ci}), the w_{ci} reduces as the surface warms. During El Niño events (Figure 6f-i) in the warming and the warm phase (SST in Figure 6f blue and orange lines, w_{ci} in 6 g and h), there is little WMT below the shallow surface layer, allowing the sea surface to warm. During the decay of the warm SST anomaly, w_{ci} grows, leading to surface cooling (Figure 6f green line (SST), 6i: w_{ci}).

The time series of w_{ci} (0°, 140°W, color coded according to the phase of the ENSO3.4 SST anomaly time series) show that the above examples are typical. During La Niña conditions, enhanced WMT occurs across the 22°C isotherm (blue, Figure 6j), while during El Niño conditions cross-isothermal velocity diminishes (red, Figure 6j). This is also true for other isotherms in the thermocline (not shown). The dependence of WMT on ENSO also depends on longitude (Figure 6k). While the ENSO signal of w_{ci} averaged over temperature classes are relatively weak in the far eastern extent of the basin, the area between 110-170°W shows distinct differences depending on the ENSO phase (Fig. 6k). w_{ci} is enhanced during La Niña throughout this longitude range, and reduced during El Niño.

In the thermocline, ENSO related w_{ci} modulation at 0°, 140°W is entirely due to $w_{\mathrm{ci}}^{\mathrm{vmix}}$ (Fig. 7a and b). In the transition from El Niño to neutral conditions to La Niña conditions w_{ci} strengthens and occurs at colder isotherms (Fig. 7a,b). For all times, most of the WMT occurs between 60-120 m depth (Fig. 7b). During La Niña, the region of water mass transformation expands down to 160 m (Fig. 7b, or 20-16°C, Fig. 7a).

To understand $w_{\mathrm{ci}}^{\mathrm{vmix}}$ variability we examine the vertical heat flux due to turbulence (J) and its divergence $\frac{\partial J}{\partial z}$. $w_{\mathrm{ci}}^{\mathrm{vmix}}$ is calculated as follows:

$$w_{\mathrm{ci}}^{\mathrm{vmix}} = \frac{1}{\rho c_p |\nabla T|} \frac{dJ}{dz}. \tag{10}$$

The vertical heat flux is enhanced throughout the thermocline during La Niña, and penetrates deeper in z-space (Fig. 7c, solid lines). This results in the heat flux divergence $\frac{dJ}{dz}$ penetrating into deeper layers during La Niña, whereas $\frac{dJ}{dz}$ is greatly reduced during El Niño (Fig. 7c, dashed lines).

The heat flux J calculated by the KPP mixing scheme below the mixed layer is dependent on both the vertical temperature gradient and the diffusivity κ:

$$J = \kappa \frac{dT}{dz}. \tag{11}$$

Comparing the temperature structure among ENSO phases reveals that the temperature gradient contribution to the heat flux J is reduced during La Niña in most places of the water column (Fig. 7d), especially in comparison to neutral conditions. The narrow range of the maximum of the EUC is the exception, here both neutral conditions and La Niña $\frac{dT}{dz}$ are larger than during El Niño, with La Niña $\frac{dT}{dz}$ slightly larger than neutral. The latter difference, however, is small.

The prominent factor leading to increased J and $\frac{dJ}{dz}$ at the depth of the EUC maximum is the strong increase in diffusivity κ (Fig. 7e, solid lines). At depths where $\frac{dT}{dz}$ is reduced ($\approx$110-150m, Fig. 7d), the increase in κ overcomes the reduced temperature gradient and leads to an overall increase in J and $\frac{dJ}{dz}$ during La Niña.

The mean vertical current shear of the zonal velocity component (Fig. 7e, dashed lines) shows the reason for the increased κ: enhanced vertical shear penetrates deeper into the ocean column during La Niña, which favors an increase in vertical mixing (Warner and Moum 2019).

The increase in total shear squared S^2 during La Niña (Figure 8c) leads to a reduced gradient Richardson number $Ri = 0.8$ ($Ri = \frac{N^2}{S^2}$, where N is the Brunt-Väisälä frequency, and S is the vertical velocity shear, Fig. 8e), which can enable mixing. In POP shear mixing is implemented below values of $Ri = 0.8$ (second gray dashed line in Figure 8e), rather than the usual value of $Ri = 0.25$ (first gray dashed line in Figure 8e). The enhanced vertical shear stems mostly from the zonal component of the flow (Fig. 8a and b).

We note that in addition to the increased shear and slightly reduced mean stability, POP frequently produces convective mixing events due to density inversions during La Niña phases (25% of the time during La Niña as compared to 8% of the time during El Niño and 10% during neutral conditions, diagnosed from a shorter run with hourly output, not shown). This strong mixing enhances the mean diffusivity. Since we cannot be certain that these events occur with similar frequency in the real world (they might be a result of the model numerical scheme), we have tested

whether filtering out all occurrences of strong convective mixing influences the results, and find that the dependence of w_{ci} on ENSO phase remains the same (not shown).

4. Discussion and Conclusions

In this study we calculate cross-isothermal velocities w_{ci} from high temporal and horizontal resolution (5-day averages, 0.1°) global ocean model output. The model has been forced with realistic surface fluxes to calculate climatological mean w_{ci} from 5-day averaged heat budget terms and w_{ci} modulation during ENSO phases.

Our methodology allows description of how w_{ci} varies in space across and along the equator, which physical processes lead to local water mass transformation (WMT), and how it is modulated during large scale changes. Here, we focus on how physical regime changes related to ENSO modulate WMT at 0°, 140°W. In the thermocline, where the three-dimensional temperature gradient is largely vertical, cross-isothermal velocities (w_{ci}) describe diabatic vertical motion, which can be separated from the adiabatic displacement of parcels along isotherms. The diabatic component of vertical motion makes up to a third of the total vertical motion, which leaves two thirds as adiabatic vertical flow (Fig. 2e). This partitioning holds in the mean, as well as for the different ENSO phases, during which Eulerian vertical velocities are modulated similarly to diabatic velocities (not shown).

These results compare well to Bryden and Brady (1985) and Meinen et al. (2001). Bryden and Brady (1985) find that 1/3 of upward transport crosses the 23°C isotherm; Meinen et al. (2001) find a similar fraction. On the other hand, Weisberg and Qiao (2000) report diapycnal transport at a rate similar to the kinematic transport, but note that this estimate is based on velocity and isotherm slopes sampled at different scales, which might lead to larger error margins. Their point estimates are larger than our values at 0°, 140°W. In contrast to the large estimate derived by Weisberg

and Qiao (2000), Brown and Fedorov (2010) find that the contribution of diapycnal transport to inter-annual variability is negligible, while they find non-negligible values in the mean. We find a significant fraction of the total velocity to be cross-isothermal, as well as distinct modulation during ENSO phases. Brown and Fedorov (2010) used a coarser ocean model with less vertical layers (36 as opposed to 62 in POP2) and a different parameterization scheme for the ocean vertical mixing. Furthermore, the shear in Brown and Fedorov (2010) is biased low, which reduces shear driven mixing. This might explain some of the differences, and highlights the importance of testing the robustness of results on diapycnal / diathermal processes in different models.

Averaging POP2 w_{ci} over the box used in (Meinen et al. 2001), i.e. 5°S-5°N, 155°W-95°W, yields values of the same order of magnitude, but a little larger than what Meinen et al. (2001) found (Fig. 9). The sign of the mean w_{ci} in our analysis is always positive, in contrast to the observational studies cited above, which find mean downwelling w_{ci} below depths of 100 m (Fig. 9). This discrepancy exists in the Eulerian mean w, as well. The model simulation does not produce mean downwelling below the EUC. We demonstrate in this manuscript that w_{ci} in the thermocline is driven by the divergence of the vertical mixing induced heat flux J. For w_{ci} to change sign again, J would have to increase below the EUC, for which an energy source would be required. We note that there are instantaneous values of downwelling, both in w (not shown) and w_{ci} (Fig.6j).

We present the cross-isothermal velocity w_{ci} in temperature space. In depth space, long term averages of this signal would be blurred by the large adiabatic vertical excursions of isopycnal from thermocline heave. The 22°C isotherm, for example, almost always lies in the thermocline, while the depth of the thermocline (and therefore the depth of the 22°C isotherm) varies from about 70m to 170m (see contours in Fig 2a,b for the depth differences of the 22°C isotherms between El Niño and La Niña). For shallower isotherms, w_{ci} as a function of temperature can only be calculated when those isotherms exist (see Fig. 10c). To create a quantity that can be compared

to the Eulerian w with units of ms^{-1}, we calculate the cumulative displacement of individual isotherms owing to diabatic processes over a specified period of time, and then divide by the length of that time period. In the thermocline, where the isotherms are always present, this does not affect the results. Close to the surface, where (warm) isotherms occur intermittently, averaging over the entire record length means that cumulative transformations across these temporary isotherms may count little for the total displacement of water, depending on how long they exist in the record. We include a comparison between the two averages, averaging over the time the isotherm exists only (Figure 10a), and the entire record length (Figure 10b). The difference is largest in the warmest layers, where isotherms may only exist during a small fraction of the total simulation (Figure 10c). For long term records it makes sense to account for the cumulative effect of WMT. However, during a field campaign of limited duration, one might expect results rather like Figure 10a than b.

We investigate the physical drivers that lead to cross-isothermal motion in the eastern equatorial Pacific. In the shallowest layer, cross-isothermal velocities become meridional rather than vertical, according to the horizontal direction of the temperature gradient. In this layer, two large effects tend to cancel: downward solar penetration decreases with depth, inducing positive (in this region poleward) $w_{\mathrm{ci}}^{\mathrm{solar}}$. "Vertical" mixing in the shallowest layer acts against this effect, acting to move warmer water "down" (equatorward; note blue shading in Fig. 4b). $w_{\mathrm{ci}}^{\mathrm{solar}}$ dominates, resulting in WMT along the temperature gradient (transformation from low to high temperatures). This balancing of solar penetration and mixing has also been stressed by Iudicone et al. (2008) and Lengaigne et al. (2012).

In the thermocline, at 140°W nominally at temperatures of 18-25°C, $w_{\mathrm{ci}}^{\mathrm{vmix}}$ is the dominant contributor to w_{ci}, and therefore drives the bulk of WMT. $w_{\mathrm{ci}}^{\mathrm{vmix}}$ changes sign from the surface to the interior, because the gradient of the heat flux due to vertical mixing changes sign: J increases with depth until $\approx$30 m, then decreases downward. The gradient of J indicates the sign and

strength of WMT due to vertical mixing (see the first term on the RHS of (9)). In the shallowest (warmest) layer, the effect of $w_{\mathrm{ci}}^{\mathrm{vmix}}$ is that water crosses mean isotherms from warm to cold, but in the thermocline $w_{\mathrm{ci}}^{\mathrm{vmix}}$ crosses mean isotherms from cold to warm.

Horizontal diffusion, eddy rectification, and higher order term effects on w_{ci} are orders of magnitude smaller than $w_{\mathrm{ci}}^{\mathrm{solar}}$ and $w_{\mathrm{ci}}^{\mathrm{vmix}}$, when basing the calculations on 5-day averages. Because the heat budget terms are averaged at each timestep and then saved as 5-daily means, the full effect of tropical instability waves (TIW) on $w_{\mathrm{ci}}^{\mathrm{vmix}}$ is resolved, rather than represented by an "eddy mixing" parameterization one would expect represented in the eddy rectification term. The small eddy rectification term in our calculation only comprises sub-5-day eddies, which are weak (not shown). With the 5-day averaged heat budget terms we resolve the mixing that results from eddy stirring induced by TIW. TIW increase vertical mixing due to increasing temperature gradients and current shear (Holmes and Thomas 2015). Separation of the effect of TIW would be possible, but requires different averaging windows. We note that the TIW in this model are weaker than observed by a factor of two. This is despite the relatively realistic representation of the EUC (Fig. 1). Rather it is due to a weak south equatorial counter current north of the equator and a weak equatorial counter current (not shown). This is at least partly attributed to deficiencies in the representation of wind stress curl in the JRA-55do forcing product (Sun et al. 2019). These errors in forcing result in a weak meridional shear north of the equator which in turn leads to reduced instability. However, we note that there are significant asymmetries across the equator indicating the TIWs are present. For instance,in Figs. 5e-g positive w_{ci} extend further north of the equator than south, especially in Fig. 5g. This is consistent with TIWs being more active during La Niña than during El Niño. The same argument holds for Fig. 6c. Modulation of w_{ci} on sub-annual time scales, such as with TIW and the seasonal cycle, are the subject of a future study.

We find that w_{ci} increases overall during La Niña because of enhanced shear due to the large scale adjustments of the circulation: strengthening of the EUC (Fig. 8b), and relatively strong westward surface currents. Stability throughout the column is reduced, with only a thin stable layer in the EUC core during La Niña (Figure 8e). The combined effect of increased shear and reduced stability leads to decreased Richardson number, with consequently enhanced vertical mixing. These results are consistent with Lengaigne et al. (2012), who found that diabatic processes contribute more than 70 % to the build up of water water volume leading to La Niña events.

During El Niño, WMT almost entirely collapses, leaving a larger role to play for adiabatic processes. Eastward surface current anomalies reduce vertical shear above the EUC core, while warmer upper-layer temperatures increase stability. These results indicate that the heat uptake in the cold tongue, which has been argued to play a dominant role in closing the heat and water mass transformation budget of the global ocean (Newsom and Thompson 2018; Holmes et al. 2019b), occurs mainly during La Niña and normal years, and is significantly diminished during El Niño. Observational evidence for the reduced heat flux during El Niño has recently been shown by Warner and Moum (2019).

This analysis points to the importance of vertical mixing, which is a parameterized process in climate models. The estimates presented here for w_{ci} and turbulent heat flux variability agrees well with the limited literature available (Holmes et al. 2019a; Huguenin et al. 2020). However, more observational constraints are necessary to quantify these vital processes, build confidence in the parameterizations, and improve upon them. Vertically resolved profiles between 2°S-2°N extending to at least 150 m depth of temperature, velocity, and, importantly, turbulent heat flux are needed to verify and validate our model.

References

Barnston, A. G., Tippett, M. K., L'Heureux, M. L., Li, S., and DeWitt, D. G. (2012). Skill of real-time seasonal enso model predictions during 2002–11: Is our capability increasing? *Bulletin of the American Meteorological Society*, 93(5):631–651.

Bayr, T., Domeisen, D. I., and Wengel, C. (2019). The effect of the equatorial pacific cold sst bias on simulated enso teleconnections to the north pacific and california. *Climate Dyn.*, 53(7-8):3771–3789.

Boyer, T. e. a. (2013). World ocean database 2013. Technical report, NOAA Atlas NESDIS 72.

Brown, J. N. and Fedorov, A. V. (2010). Estimating the diapycnal transport contribution to warm water volume variations in the tropical pacific ocean. *Journal of climate*, 23(2):221–237.

Bryan, F. and Bachman, S. (2015). Isohaline salinity budget of the north atlantic salinity maximum. *Journal of Physical Oceanography*, 45(3):724–736.

Bryden, H. L. and Brady, E. C. (1985). Diagnostic model of the three-dimensional circulation in the upper equatorial pacific ocean. *Journal of Physical Oceanography*, 15(10):1255–1273.

Chang, P., Yamagata, T., Schopf, P., Behera, S., Carton, J., Kessler, W., Meyers, G., Qu, T., Schott, F., Shetye, S., et al. (2006). Climate fluctuations of tropical coupled systems—the role of ocean dynamics. *Journal of Climate*, 19(20):5122–5174.

Chassignet, E. P., Yeager, S. G., Fox-Kemper, B., and etal (2020). Impact of horizontal resolution of global ocean-sea-ice model simulations based on the experimental protocols of the ocean model intercomparison project phase 2 (omip-2). *Geoscientific Model Development*, page in press.

Cromwell, T. (1953). Circulation in a meridional plane in the central equatorial pacific. *Journal of Marine Research*, 12:196–213.

Cromwell, T., Montgomery, R. B., and D, S. E. (1954). Equatorial undercurrent in pacific ocean revealed by new methods. *Science*, 119:648–649.

Ding, H., Newman, M., Alexander, M. A., and Wittenberg, A. T. (2020). Relating cmip5 model biases to seasonal forecast skill in the tropical pacific. *Geophys. Res. Lett.*, 47(5):e2019GL086765.

England, M. H., McGregor, S., Spence, P., Meehl, G. A., Timmermann, A., Cai, W., Gupta, A. S., McPhaden, M. J., Purich, A., and Santoso, A. (2014). Recent intensification of wind-driven circulation in the pacific and the ongoing warming hiatus. *Nature climate change*, 4(3):222–227.

Groeskamp, S., Griffies, S. M., Iudicone, D., Marsh, R., Nurser, A. G., and Zika, J. D. (2019). The water mass transformation framework for ocean physics and biogeochemistry. *Annual review of marine science*, 11:271–305.

Hieronymus, M., Nilsson, J., and Nycander, J. (2014). Water mass transformation in salinity–temperature space. *Journal of Physical Oceanography*, 44(9):2547–2568.

Holmes, R. and Thomas, L. (2015). The modulation of equatorial turbulence by tropical instability waves in a regional ocean model. *Journal of Physical Oceanography*, 45(4):1155–1173.

Holmes, R. M., Zika, J. D., and England, M. H. (2019a). Diathermal heat transport in a global ocean model. *Journal of Physical Oceanography*, 49(1):141–161.

Holmes, R. M., Zika, J. D., Ferrari, R., Thompson, A. F., Newsom, E. R., and England, M. H. (2019b). Atlantic ocean heat transport enabled by indo-pacific heat uptake and mixing. *Geophysical Research Letters*, 46(23):13939–13949.

Huguenin, M. F., Holmes, R. M., and England, M. H. (2020). Key role of diabatic processes in regulating warm water volume variability over enso events. *Journal of Climate*, 33(22):9945–9964.

Iudicone, D., Madec, G., and McDougall, T. J. (2008). Water-mass transformations in a neutral density framework and the key role of light penetration. *Journal of Physical Oceanography*, 38(7):1357–1376.

Ji, M. and Leetmaa, A. (1997). Impact of data assimilation on ocean initialization and el nino prediction. *Monthly Weather Review*, 125(5):742–753.

Jin, F.-F. (1997). An equatorial ocean recharge paradigm for enso. part i: Conceptual model. *Journal of the atmospheric sciences*, 54(7):811–829.

Johnson, G. C., McPhaden, M. J., and E, F. (2001). Equatorial pacific ocean horizontal velocity, divergence, and upwelling. *Journal of Physical Oceanography*, 31:839—-848.

Karnauskas, K. B., Murtugudde, R., and Busalacchi, A. J. (2007). The effect of the galápagos islands on the equatorial pacific cold tongue. *Journal of physical oceanography*, 37(5):1266–1281.

Kobayashi, S., Ota, Y., Harada, Y., Ebita, A., Moriya, M., Onoda, H., Onogi, K., Kamahori, H., Kobayashi, C., Endo, H., et al. (2015). The jra-55 reanalysis: General specifications and basic characteristics. *Journal of the Meteorological Society of Japan. Ser. II*, 93(1):5–48.

Large, W. G., McWilliams, J. C., and Doney, S. C. (1994). Oceanic vertical mixing: A review and a model with a nonlocal boundary layer parameterization. *Reviews of Geophysics*, 32(4):363–403.

Lengaigne, M., Hausmann, U., Madec, G., Menkès, C., Vialard, J., and Molines, J.-M. (2012). Mechanisms controlling warm water volume interannual variations in the equatorial pacific: diabatic versus adiabatic processes. *Climate Dynamics*, 38(5-6):1031–1046.

Lien, R.-C., Caldwell, D. R., Gregg, M., and Moum, J. N. (1995). Turbulence variability at the equator in the central pacific at the beginning of the 1991–1993 el nino. *Journal of Geophysical Research: Oceans*, 100(C4):6881–6898.

McPhaden, M. J., Zebiak, S. E., and Glantz, M. H. (2006). Enso as an integrating concept in earth science. *science*, 314(5806):1740–1745.

Mechoso, C. R., Robertson, A. W., Barth, N., Davey, M., Delecluse, P., Gent, P., Ineson, S., Kirtman, B., Latif, M., Treut, H. L., et al. (1995). The seasonal cycle over the tropical pacific in coupled ocean–atmosphere general circulation models. *Monthly Weather Review*, 123(9):2825–2838.

Meinen, C., McPhaden, M. J., and Johnson, G. C. (2001). Vertical velocities and transports in the equatorial pacific during 1993-99. *Journal of Physical Oceanography*, 31:3230–3248.

Meinen, C. S. and McPhaden, M. J. (2000). Observations of warm water volume changes in the equatorial pacific and their relationship to el niño and la niña. *Journal of Climate*, 13(20):3551–3559.

Meinen, C. S. and McPhaden, M. J. (2001). Interannual variability in warm water volume transports in the equatorial pacific during 1993–99. *Journal of physical oceanography*, 31(5):1324–1345.

Moum, J. and Nash, J. (2009). Mixing measurements on an equatorial ocean mooring. *Journal of Atmospheric and Oceanic Technology*, 26(2):317–336.

514 Moum, J. N., Caldwell, D. R., and Paulson, C. A. (1989). Mixing in the equatorial surface layer
515 and thermocline. *Journal of Geophysical Research: Oceans*, 94(C2):2005–2022.

516 Moum, J. N., Perlin, A., Nash, J. D., and McPhaden, M. J. (2013). Seasonal sea surface cooling
517 in the equatorial pacific cold tongue controlled by ocean mixing. *Nature*, 500(7460):64–67.

518 Neelin, J. D., Battisti, D. S., Hirst, A. C., Jin, F.-F., Wakata, Y., Yamagata, T., and Zebiak, S. E.
519 (1998). Enso theory. *Journal of Geophysical Research: Oceans*, 103(C7):14261–14290.

520 Newsom, E. R. and Thompson, A. F. (2018). Reassesing the role of the indo-pacific in the ocean's
521 global overturning circulation. *Geophysical Research Letters*, 45:12,422–12,431.

522 Niiler, P. and Stevenson, J. (1982). The heat budget of tropical ocean warm-water pools. *J. Mar.*
523 *Res*, 40:465–480.

524 Nurser, A., Marsh, R., and Williams, R. G. (1999). Diagnosing water mass formation from air–sea
525 fluxes and surface mixing. *Journal of physical oceanography*, 29(7):1468–1487.

526 Ohlmann, J. C. (2003). Ocean radiant heating in climate models. *Journal of Climate*, 16(9):1337–
527 1351.

528 Philander, S. G. H. (1990). *El Nino, La Nina, and the Southern Oscillation*. Academic Press, San
529 Diego.

530 Ray, S., Wittenberg, A. T., Griffies, S. M., and Zeng, F. (2018). Understanding the equatorial
531 pacific cold tongue time-mean heat budget. part ii: Evaluation of the gfdl-flor coupled gcm.
532 *Journal of Climate*, 31(24):9987–10011.

533 Samanta, D., Karnauskas, K. B., and Goodkin, N. F. (2019). Tropical pacific sst and itcz biases in
534 climate models: Double trouble for future rainfall projections? *Geophys. Res. Lett.*, 46(4):2242–
535 2252.

Smith, R., Jones, P., Briegleb, B., Bryan, F., Danabasoglu, G., Dennis, J., Dukowicz, J., Eden, C., Fox-Kemper, B., Gent, P., et al. (2010). The parallel ocean program (pop) reference manual: Ocean component of the community climate system model (ccsm). *Los Alamos Natl Lab LAUR-10-01853*.

Smyth, W. and Moum, J. (2013). Marginal instability and deep cycle turbulence in the eastern equatorial pacific ocean. *Geophysical Research Letters*, 40(23):6181–6185.

Sun, Z., Liu, H., Lin, P., Tseng, Y.-h., Small, J., and Bryan, F. (2019). The modeling of the north equatorial countercurrent in the community earth system model and its oceanic component. *Journal of Advances in Modeling Earth Systems*, 11(2):531–544.

Tang, Y., Zhang, R.-H., Liu, T., Duan, W., Yang, D., Zheng, F., Ren, H., Lian, T., Gao, C., Chen, D., et al. (2018). Progress in enso prediction and predictability study. *National Science Review*, 5(6):826–839.

Timmermann, A., An, S.-I., Kug, J.-S., Jin, F.-F., Cai, W., Capotondi, A., Cobb, K. M., Lengaigne, M., McPhaden, M. J., Stuecker, M. F., et al. (2018). El niño–southern oscillation complexity. *Nature*, 559(7715):535–545.

Toole, J. M., Zhang, H.-M., and Caruso, M. J. (2004). Time-dependent internal energy budgets of the tropical warm water pools. *Journal of climate*, 17(6):1398–1410.

Tsujino, H., Urakawa, S., Nakano, H., Small, R. J., Kim, W. M., Yeager, S. G., Danabasoglu, G., Suzuki, T., Bamber, J. L., Bentsen, M., et al. (2018). Jra-55 based surface dataset for driving ocean–sea-ice models (jra55-do). *Ocean Modelling*, 130:79–139.

Viúdez, A. (2001). Volume and mass transport across isosurfaces of a balanced fluid property. *Journal of Physical Oceanography*, 30:1478–1485.

Walin, G. (1982). On the relation between sea-surface heat flow and thermal circulation in the ocean. *Tellus*, 34:187–195.

Wang, C., Deser, C., Yu, J.-Y., DiNezio, P., and Clement, A. (2017). El niño and southern oscillation (enso): a review. In *Coral reefs of the eastern tropical Pacific*, pages 85–106. Springer.

Wang, W. and McPhaden, M. J. (1999). The surface-layer heat balance in the equatorial pacific ocean. part i: Mean seasonal cycle. *Journal of physical oceanography*, 29(8):1812–1831.

Wang, W. and McPhaden, M. J. (2000). The Surface-Layer Heat Balance in the Equatorial Pacific Ocean. Part II: Interannual Variability*. *J. Phys. Oceanogr.*, 30(11):2989–3008.

Warner, S. J. and Moum, J. N. (2019). Feedback of mixing to enso phase change. *Geophysical Research Letters*, 46(23):13920–13927.

Weisberg, R. H. and Qiao, L. (2000). Equatorial upwelling in the central pacific estimated from moored velocity profilers. *Journal of Physical Oceanography*, 30(1):105–124.

Wyrtki, K. (1975). El niño—the dynamic response of the equatorial pacific oceanto atmospheric forcing. *Journal of Physical Oceanography*, 5(4):572–584.

Wyrtki, K. (1981). An estimate of equatorial upwelling in the pacific. *Journal of Physical Oceanography*, 11:1205–1214.

Zelle, H., Appeldoorn, G., Burgers, G., and van Oldenborgh, G. J. (2004). The relationship between sea surface temperature and thermocline depth in the eastern equatorial pacific. *Journal of physical oceanography*, 34(3):643–655.

Acknowledgments. This study was supported by the National Center for Atmospheric Research, which is a major facility sponsored by the National Science Foundation under Cooperative Agree-

ment No. 1852977, and by the NOAA Climate Variability Program under Grant Agreement No. NA18OAR4310399. This work is part of the CVP TPOS 2020 pre-field modeling effort lead by Dr. Sandy Lucas, and is PMEL contribution number 5154. Computing resources were provided by the Climate Simulation Laboratory at NCAR's Computational and Information Systems Laboratory (CISL). TAO observational data were made available by the GTMBA Project Office of NOAA/PMEL and accessed through the website `https://www.pmel.noaa.gov/tao/drupal/disdel/`. The authors gratefully acknowledge Dr. Christopher Meinen for providing estimates of w_{ci} from Meinen et al. (2001), and Dr. Deepak Cherian for valuable help during the software development process.

LIST OF FIGURES

Fig. 1. POP2 and TAO temperature [°C] and velocity [cm/sec] profiles on the equator at 170°W, 140°W, and 110°W. Envelopes around the profiles show one standard deviation (all time scales). The following years have been chosen for the velocity comparison, according to TAO data availability: May 1988 until August 2018 for 170°W, May 1990 until April 2018 for 140°W, and May 1991 until April 2016 for 110°W. Gaps in TAO data have not been accounted for in sampling the model data. The total POP2 (1983-2018) and TAO records (1988-2020) have been used for the temperature comparison. We note that neither the mean nor the standard deviation of U or T significantly change when choosing shorter periods. . . . 30

Fig. 2. Sea surface temperature for exemplary El Niño (a) and La Niña years (b), with the depth of the 22°C isotherm in gray. 36 year time averages of c) cross-isothermal velocity w_{ci} in temperature space [m/day], d) Eulerian vertical velocity in depth space [m/day], isotherms in dark contours (spacing 2°C, zonal velocity in white contours (spacing 20 cm/s) across the Equator from 5°S to 5°N at 140°W, and e) profiles of cross-isothermal velocity [m/day], and Eulerian vertical [m/day] and zonal [m/sec] velocities at 0°, 140°W in depth space. Hatching in c) corresponds to isotherms that are present for less than 50 % of the time. All panels display POP2 model output and derived quantities. 31

Fig. 3. 36 year time averages of cross-isothermal velocity w_{ci} in POP2 in temperature space [m/day] as in Figure 2c) across the 22 °C isotherm in the equatorial Pacific between 3°S to 3°N and from the South American coast to 170°E. Below are cross sections for 165°W, 125°W, and 110°W, hatching indicates isotherms that exist less than 50 % of the time. 32

Fig. 4. Main drivers of the cross-isothermal velocity w_{ci} calculated according to Equation 8 from the POP2 full heat budget output, in temperature space averaged over the 36 year long time-series. Terms shown are: a) total cross-isothermal velocity w_{ci}, b) cross-isothermal velocity attributable to vertical mixing $w_{\mathrm{ci}}^{\mathrm{vmix}}$, d) solar penetration $w_{\mathrm{ci}}^{\mathrm{solar}}$, horizontal mixing, and c) the sum of $w_{\mathrm{ci}}^{\mathrm{vmix}}$ and $w_{\mathrm{ci}}^{\mathrm{solar}}$. Eddy fluxes and horizontal diffusion are not shown, they are orders of magnitude smaller than the terms shown. Hatching shows the region where isotherms exist less than 50% of the time. 33

Fig. 5. a) Niño3.4 index in the forced simulation, w_{ci} for El Niño (b), neutral conditions (c), and La Niña (d), phases marked on the ENSO3.4 time series in a). $w_{\mathrm{ci}}^{\mathrm{vmix}}$ for El Niño (e), neutral (f), and La Niña (g), and $w_{\mathrm{ci}}^{\mathrm{solar}}$ for El Niño (h), neutral (i), and La Niña (j). w_{ci} is calculated according to Equation 9, $w_{\mathrm{ci}}^{\mathrm{vmix}}$ and $w_{\mathrm{ci}}^{\mathrm{solar}}$ are calculated from the second and first terms of the RHS of Equation 8, respectively. All panels display POP2 model output and derived quantities. 34

Fig. 6. Examples of w_{ci} modulation with ENSO in POP2 at 140°W during La Niña (a-d), El Niño (f-i). Panels a and f show the SST time series of the event, separated into build up (blue), maintenance (orange), and discharge (green) periods. Horizontal lines in (b-d) and (g-i) show the location of the 22°C isotherm, and the vertical line shows the equator, for orientation. Panel j shows the 5-day time series of cross-isothermal velocity across the 22°C isotherm at 0°, 140°W, panel k shows the dependence of cross-isothermal velocity modulation [m/day] on longitude in the form of column averages for the different phases along the equator. Vertical lines denote the locations 125°W, 140°W, 155°W, 170°W, and 180°, for orientation. 35

Fig. 7. POP2 profiles at 0°, 140°W for El Niño (red), La Niña (blue), and neutral (black) conditions. a) and b) show cross-isothermal velocity in temperature and depth space, respectively. c) shows the flux due to vertical mixing (solid, [w/m^2]) and its divergence (dashed; [w/m^3]),

d) shows the vertical temperature gradient [°C/cm], and e) shows model diffusivity κ (solid, [m^2/s]) and the absolute mean vertical shear of the zonal velocity (dashed; [1/s]). 36

Fig. 8. POP2 profiles at 0°, 140°W for El Niño (red), La Niña (blue), and neutral (black) conditions. a) and b) show meridional and zonal velocity components, respectively. c) and d) show total shear squared and buoyancy squared, from which the gradient Richardson number Ri is calculated, shown in e) and zoomed in on the upper 100 m in f). Dashed horizontal lines show the depth of the EUC maximum per ENSO phase. 37

Fig. 9. Comparison w_{ci} over the Meinen et al. (2001) box 5°S-5°N, 155°W-95°W in temperature space (values from Meinen et al. (2001) Figure 9 provided by C. Meinen). 38

Fig. 10. 36 year average of the total cross-isothermal velocity at 140W across the equator. (a) shows an average that takes into account each point only when the isotherm exists, which leads to larger values close to the surface where isotherms are present only during some periods. (b) shows the total sum of w_{ci} at a given point divided by the entire record length, regardless of whether that isotherm exists at all times. (c) shows the amount of time a given isotherm exists throughout the record at 0°, 140°W, left y-axis in years and right y-axis in percent of time. (d) illustrates the difference of w_{ci} at 0°, 140°W between the two averaging methods. All panels display derived quantities from POP2 model output. 39

FIG. 1. POP2 and TAO temperature [°C] and velocity [cm/sec] profiles on the equator at 170°W, 140°W, and 110°W. Envelopes around the profiles show one standard deviation (all time scales). The following years have been chosen for the velocity comparison, according to TAO data availability: May 1988 until August 2018 for 170°W, May 1990 until April 2018 for 140°W, and May 1991 until April 2016 for 110°W. Gaps in TAO data have not been accounted for in sampling the model data. The total POP2 (1983-2018) and TAO records (1988-2020) have been used for the temperature comparison. We note that neither the mean nor the standard deviation of U or T significantly change when choosing shorter periods.

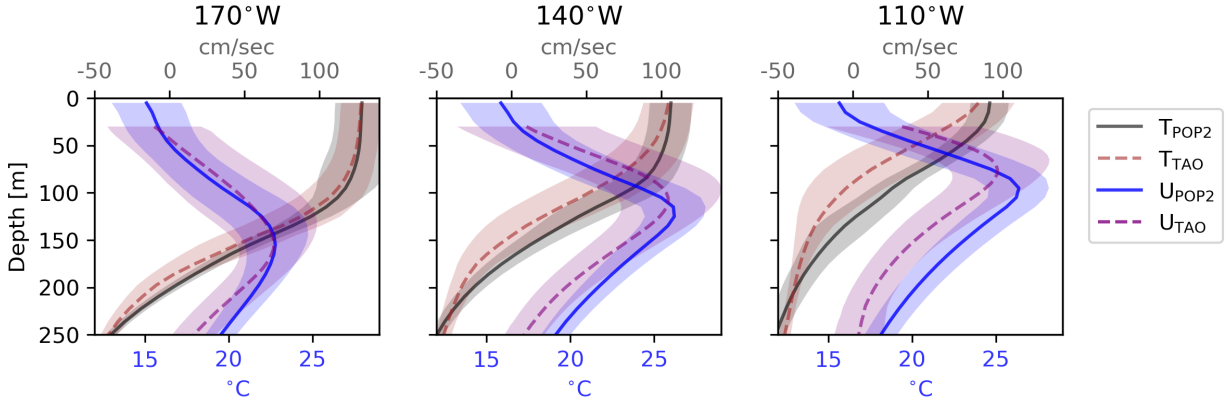

FIG. 2. Sea surface temperature for exemplary El Niño (a) and La Niña years (b), with the depth of the 22°C isotherm in gray. 36 year time averages of c) cross-isothermal velocity w_{ci} in temperature space [m/day], d) Eulerian vertical velocity in depth space [m/day], isotherms in dark contours (spacing 2°C, zonal velocity in white contours (spacing 20 cm/s) across the Equator from 5°S to 5°N at 140°W, and e) profiles of cross-isothermal velocity [m/day], and Eulerian vertical [m/day] and zonal [m/sec] velocities at 0°, 140°W in depth space. Hatching in c) corresponds to isotherms that are present for less than 50 % of the time. All panels display POP2 model output and derived quantities.

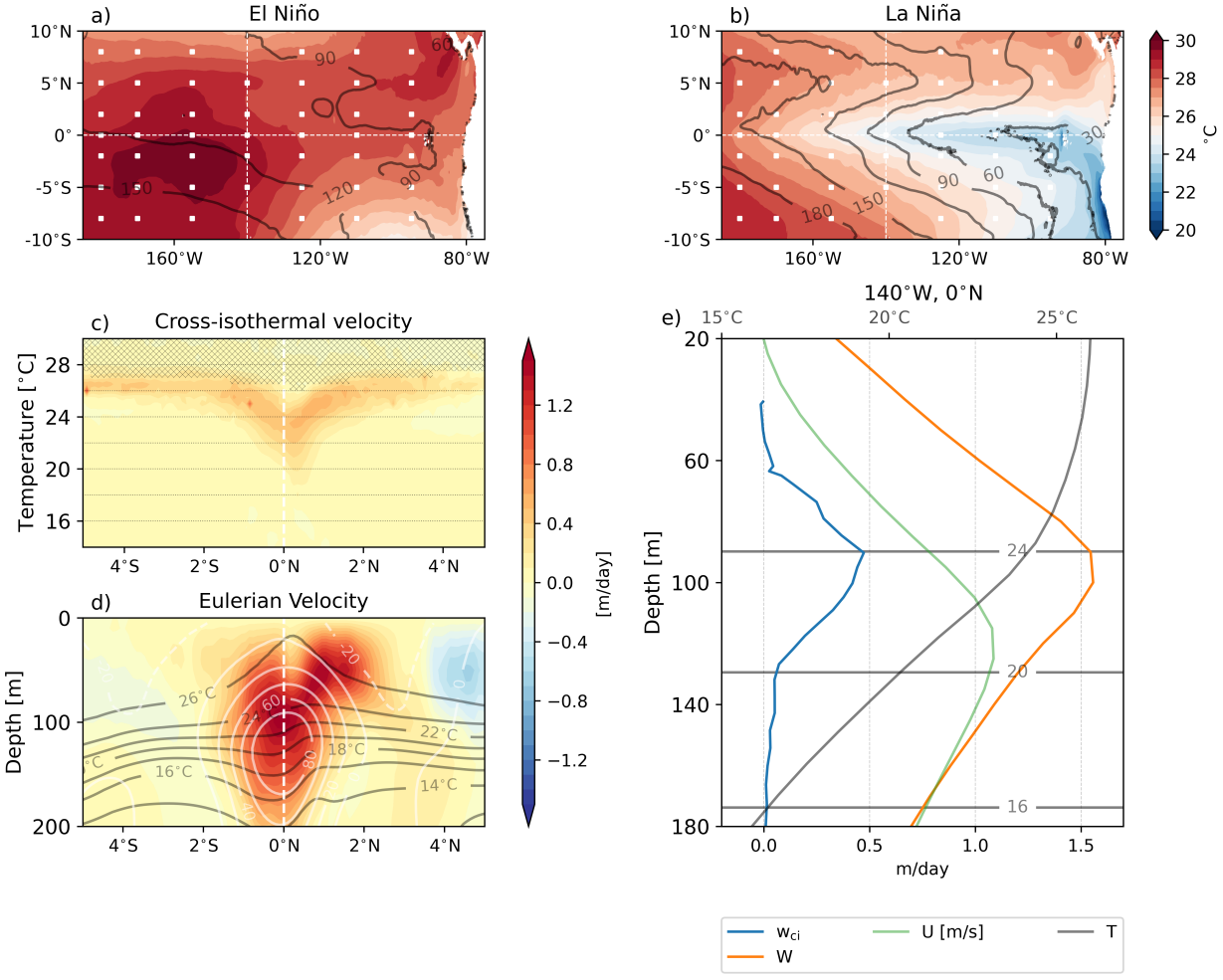

FIG. 3. 36 year time averages of cross-isothermal velocity w_{ci} in POP2 in temperature space [m/day] as in Figure 2c) across the 22 °C isotherm in the equatorial Pacific between 3°S to 3°N and from the South American coast to 170°E. Below are cross sections for 165°W, 125°W, and 110°W, hatching indicates isotherms that exist less than 50 % of the time.

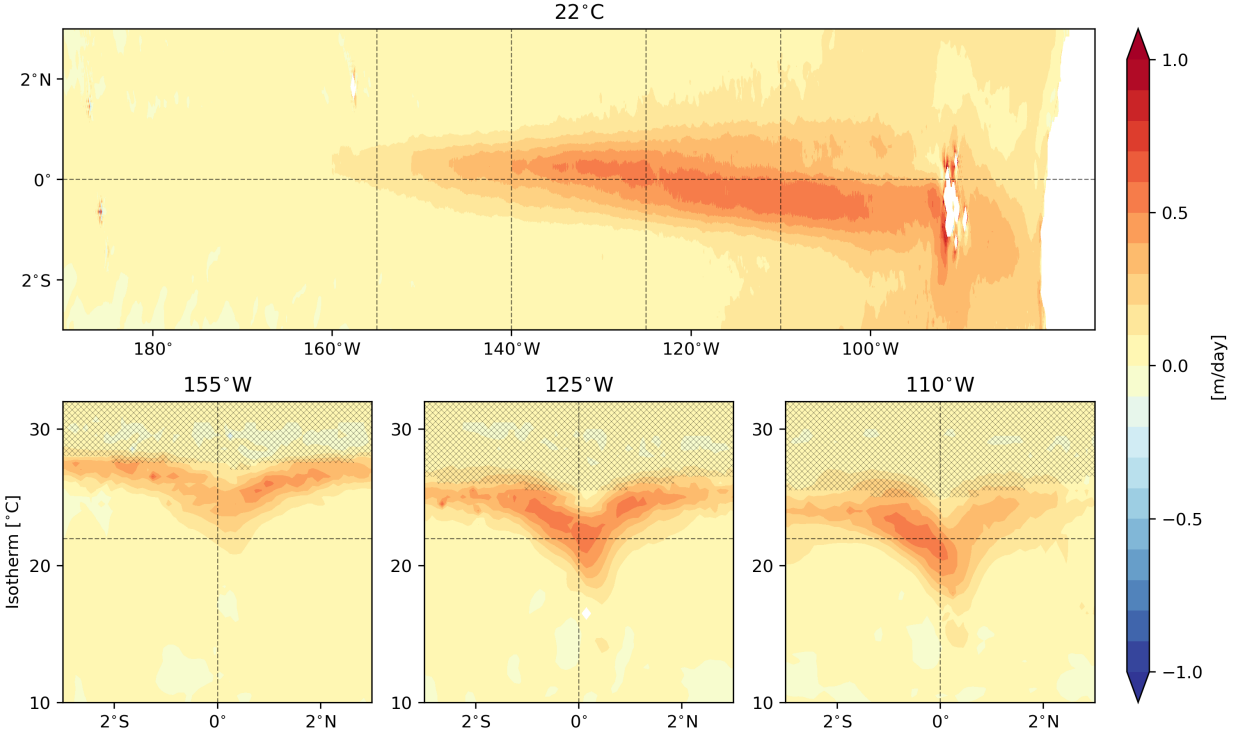

669 FIG. 4. Main drivers of the cross-isothermal velocity w_{ci} calculated according to Equation 8 from the POP2
670 full heat budget output, in temperature space averaged over the 36 year long time-series. Terms shown are: a)
671 total cross-isothermal velocity w_{ci}, b) cross-isothermal velocity attributable to vertical mixing $w_{\mathrm{ci}}^{\mathrm{vmix}}$, d) solar
672 penetration $w_{\mathrm{ci}}^{\mathrm{solar}}$, horizontal mixing, and c) the sum of $w_{\mathrm{ci}}^{\mathrm{vmix}}$ and $w_{\mathrm{ci}}^{\mathrm{solar}}$. Eddy fluxes and horizontal diffusion
673 are not shown, they are orders of magnitude smaller than the terms shown. Hatching shows the region where
674 isotherms exist less than 50% of the time.

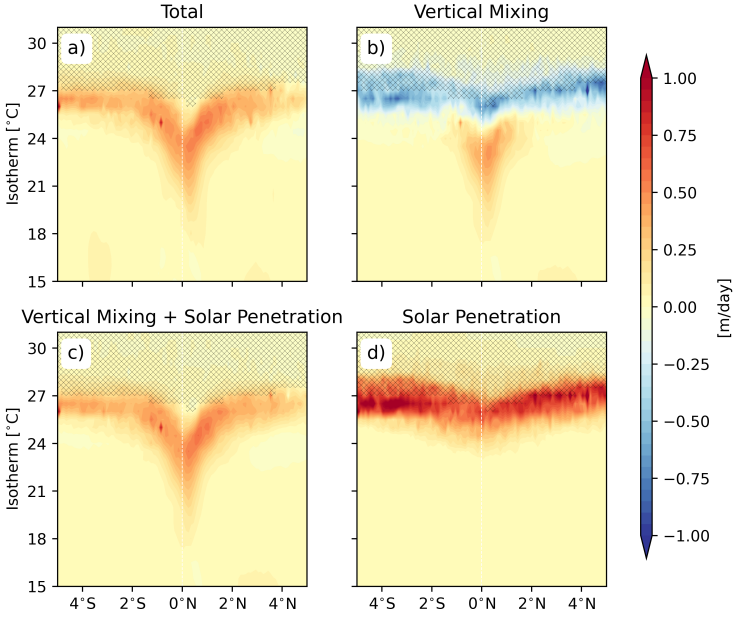

FIG. 5. a) Niño3.4 index in the forced simulation, w_{ci} for El Niño (b), neutral conditions (c), and La Niña (d), phases marked on the ENSO3.4 time series in a). $w_{\mathrm{ci}}^{\mathrm{vmix}}$ for El Niño (e), neutral (f), and La Niña (g), and $w_{\mathrm{ci}}^{\mathrm{solar}}$ for El Niño (h), neutral (i), and La Niña (j). w_{ci} is calculated according to Equation 9, $w_{\mathrm{ci}}^{\mathrm{vmix}}$ and $w_{\mathrm{ci}}^{\mathrm{solar}}$ are calculated from the second and first terms of the RHS of Equation 8, respectively. All panels display POP2 model output and derived quantities.

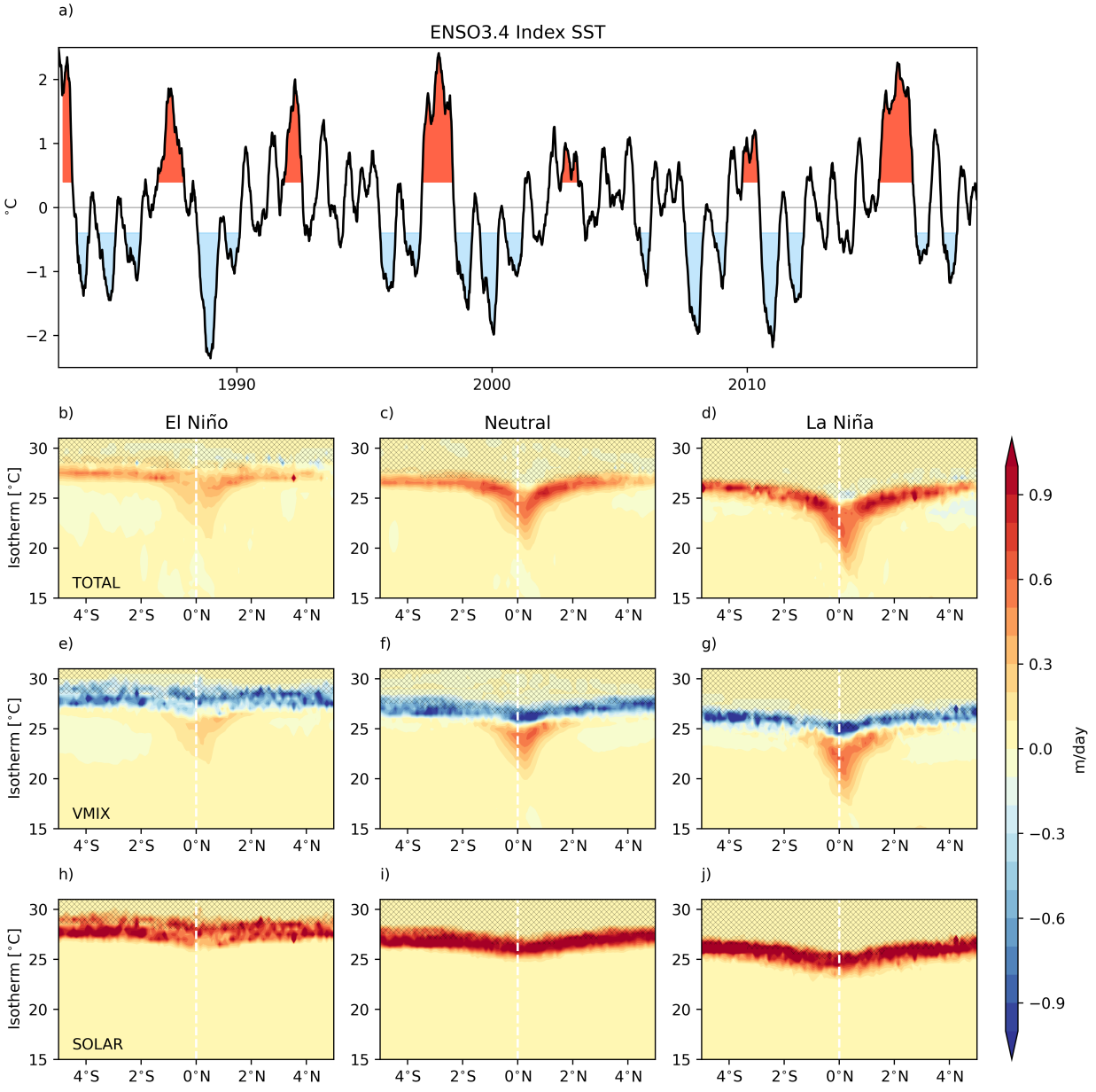

FIG. 6. Examples of w_{ci} modulation with ENSO in POP2 at 140°W during La Niña (a-d), El Niño (f-i). Panels a and f show the SST time series of the event, separated into build up (blue), maintenance (orange), and discharge (green) periods. Horizontal lines in (b-d) and (g-i) show the location of the 22°C isotherm, and the vertical line shows the equator, for orientation. Panel j shows the 5-day time series of cross-isothermal velocity across the 22°C isotherm at 0°, 140°W, panel k shows the dependence of cross-isothermal velocity modulation [m/day] on longitude in the form of column averages for the different phases along the equator. Vertical lines denote the locations 125°W, 140°W, 155°W, 170°W, and 180°, for orientation.

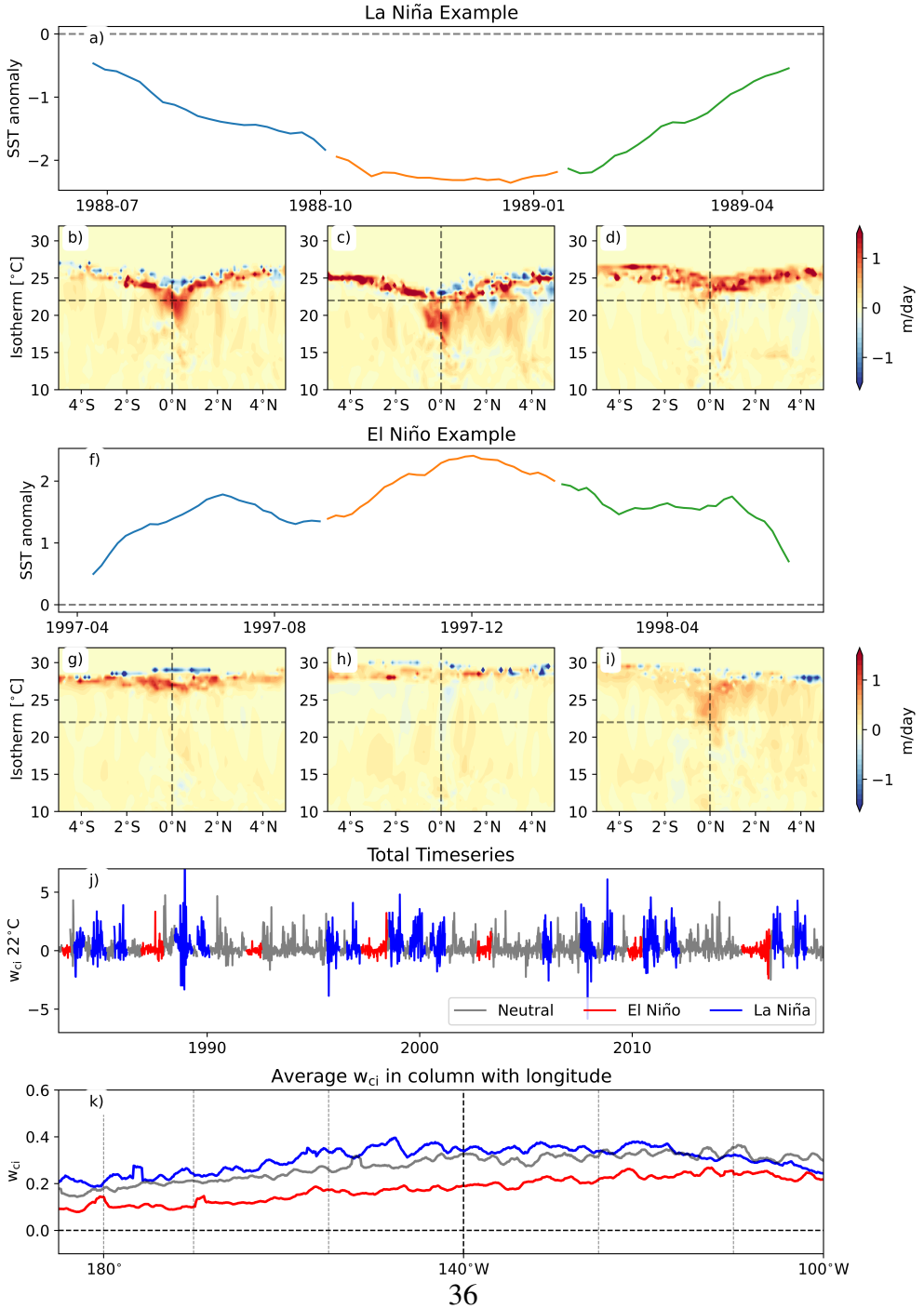

FIG. 7. POP2 profiles at 0°, 140°W for El Niño (red), La Niña (blue), and neutral (black) conditions. a) and b) show cross-isothermal velocity in temperature and depth space, respectively. c) shows the flux due to vertical mixing (solid, [w/m^2]) and its divergence (dashed; [w/m^3]), d) shows the vertical temperature gradient [°C/cm], and e) shows model diffusivity κ (solid, [m^2/s]) and the absolute mean vertical shear of the zonal velocity (dashed; [1/s]).

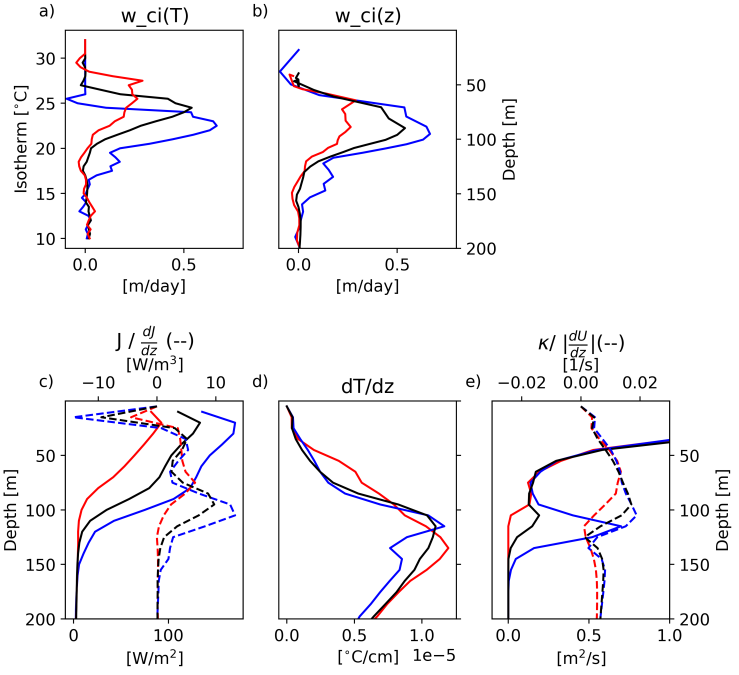

FIG. 8. POP2 profiles at 0°, 140°W for El Niño (red), La Niña (blue), and neutral (black) conditions. a) and b) show meridional and zonal velocity components, respectively. c) and d) show total shear squared and buoyancy squared, from which the gradient Richardson number Ri is calculated, shown in e) and zoomed in on the upper 100 m in f). Dashed horizontal lines show the depth of the EUC maximum per ENSO phase.

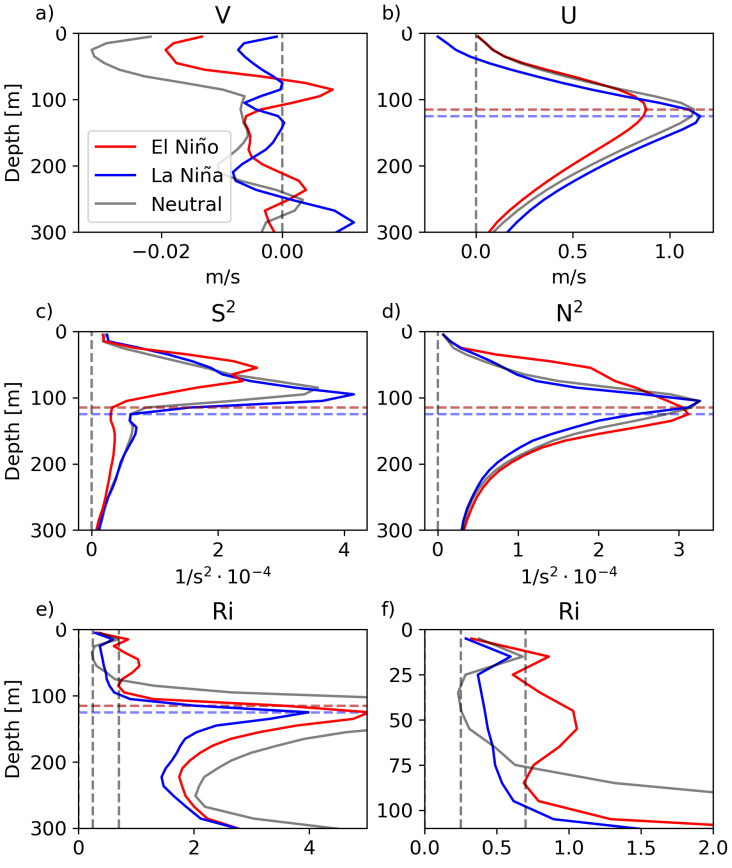

FIG. 9. Comparison w_{ci} over the Meinen et al. (2001) box 5°S-5°N, 155°W-95°W in temperature space (values from Meinen et al. (2001) Figure 9 provided by C. Meinen).

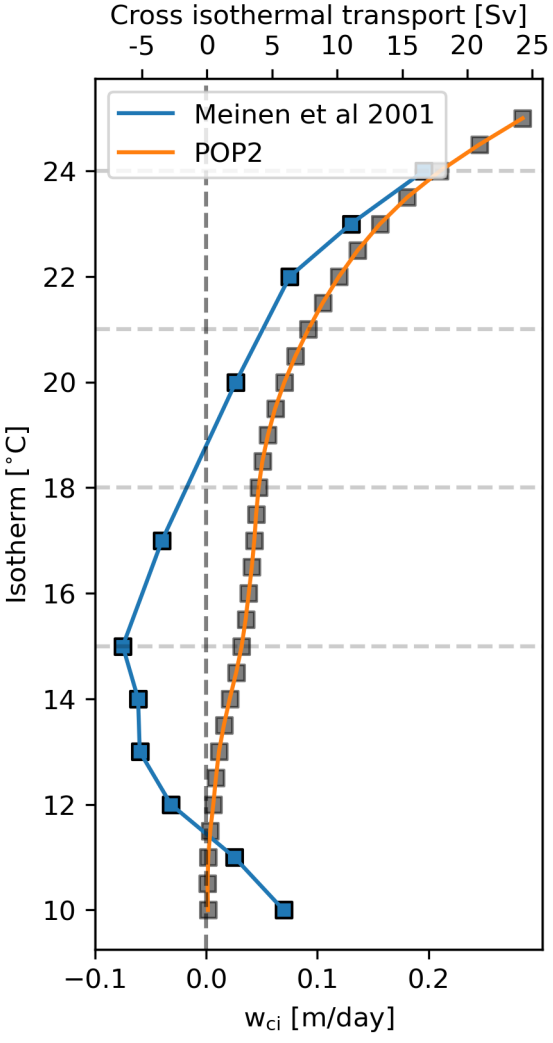
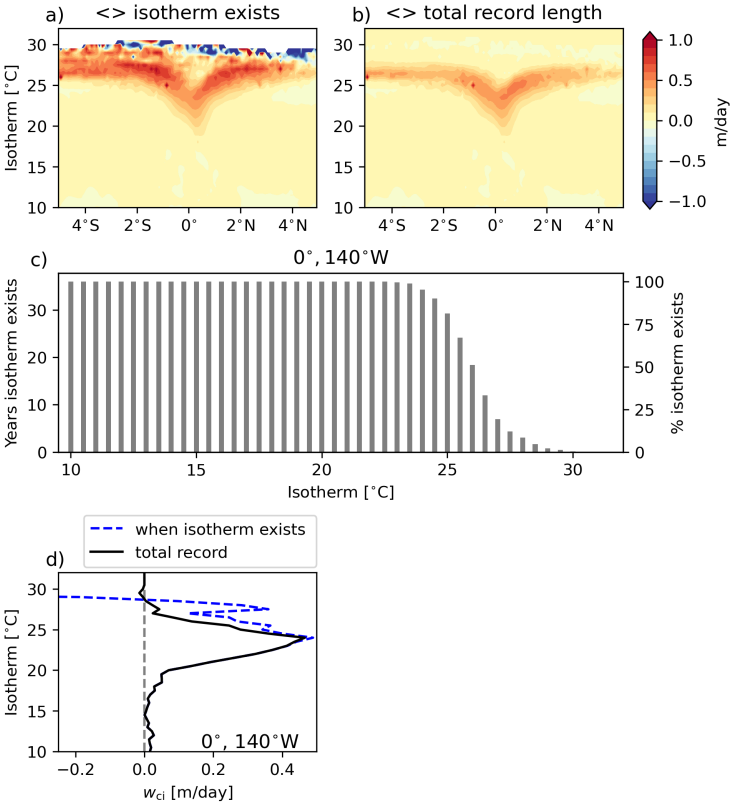
FIG. 10. 36 year average of the total cross-isothermal velocity at 140W across the equator. (a) shows an average that takes into account each point only when the isotherm exists, which leads to larger values close to the surface where isotherms are present only during some periods. (b) shows the total sum of w_{ci} at a given point divided by the entire record length, regardless of whether that isotherm exists at all times. (c) shows the amount of time a given isotherm exists throughout the record at 0°, 140°W, left y-axis in years and right y-axis in percent of time. (d) illustrates the difference of w_{ci} at 0°, 140°W between the two averaging methods. All panels display derived quantities from POP2 model output.